ACS Sustainable Chemistry & Engineering

pubs.acs.org/journal/ascecg

Research Article

Evaluation of Impurities in Aluminum Anodes for Al-Air Batteries

Jianming Ren, Chaopeng Fu,* Qing Dong, Min Jiang, Anping Dong,* Guoliang Zhu, Jiao Zhang, and Baode Sun

Cite This: *ACS Sustainable Chem. Eng.* 2021, 9, 2300−2308

Read Online

ACCESS | Metrics & More | Article Recommendations | Supporting Information

ABSTRACT: Aluminum anodes with various purity grades (2N8, 3N6, 3N8, 4N6, and 5N) are characterized and investigated as anodes for aluminum-air batteries. The effects of impurity elements (Fe, Si, Ga, Zn, etc.) and the associated microstructure change on battery performance are evaluated through microstructure and surface potential analysis and electrochemical and battery measurements. The results reveal that the decrease in contents of Fe and Si in Al anodes can alleviate the self-corrosion and boost the anode utilization. Moreover, the Al anode with a higher purity shows a more negative open-circuit potential to realize a larger open-circuit voltage for the Al-air battery, except the 3N6 Al anode. The 3N6 Al anode displays a higher electrochemical activity than the 4N6 Al anode due to the activation from Zn and Ga elements. The Al-air batteries with 5N Al and 4N6 Al display large discharge voltages and specific capacities at 20 mA cm^{-2}. The Al-air batteries with 2N8 Al and 3N8 Al exhibit better discharge characteristics than those with 5N Al and 4N6 Al at a higher current density because of smaller polarization resistances. The Al-air battery with 3N6 Al shows larger discharge voltages at both low and high current densities. Finally, the energy cost of various Al anodes is evaluated, and the result reveals that the 3N6 Al anode is the most cost-effective anode for Al-air batteries in this study.

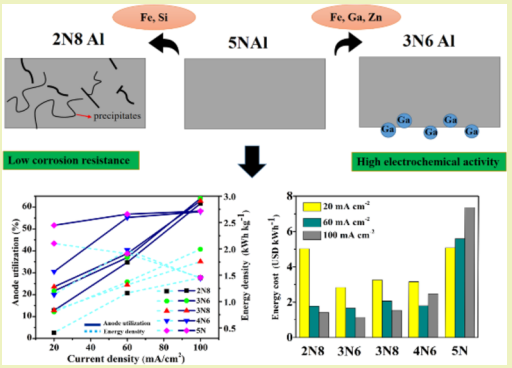

KEYWORDS: *aluminum anode, impurity, Al-air battery, electrochemistry, self-corrosion*

INTRODUCTION

Aluminum-air (Al-air) batteries have shown promising application in power stations, electrical vehicles, and large-scale energy storage systems with the merits of a high theoretical energy density (8.1 kWh kg^{-1}), a negative electrode potential (−1.66 V vs NHE), light weight, and low cost as well as abundant reserve in the nature of Al.[1−5] However, the commercialization of Al-air batteries is mainly hindered by a low utilization rate of the Al anode due to the severe self-corrosion in alkaline electrolytes,[6−10] which lowers the energy density, operating voltage, and safety of Al-air batteries. To reduce the self-corrosion of Al anodes, Al alloys with designed alloying elements are applied to achieve enhanced battery performance. The addition of alloy elements such as Mg, Zn, Ga, and Pb into pure Al for casting Al alloys is an effective way to boost the Al-air battery's performance. However, pure Al with a high purity is generally needed for alloying, which will significantly increase the cost.[11−16] Recently, Liu et al. prepared the Al−Sb alloys with different Sb fractions and studied the role of AlSb precipitates in improving the discharge performance of Al-air batteries.[17] Wu et al. revealed that the addition of indium in Al−Mg−Sn-based anodes could boost the electrochemical activity and increase the anodic efficiency.[18] Ren et al. investigated the positive role of Mg and Sn additions in suppressing the self-corrosion of Al anodes, which was also confirmed by the ab initio energy calculation based on the density functional theory.[19] Yu et al. prepared the Al anodes by laser sintering to improve electrochemical performance of the Al-air battery due to the enhancement of electrical contacts between Al nanoparticles.[20] In addition, Wu et al. developed a coarse-grained Al-0.5 Mg-0.1Sn-0.05Ga anode by a directional solidification technique in combination with a rolling process and subsequent annealing, and the anode delivered a maximum energy density of 3743.9 Wh kg^{-1}.[21] Zheng et al. reported that the Al anode processed by stir welding displayed a large voltage and energy density.[22]

Pure Al anodes show diverse battery performance due to various impurities. Pure Al is also the feedstock to produce Al alloys, and the purity can also affect performance of the formed Al alloys. Additionally, it is well known that the production price of high-grade Al (5N and 6N) is 20−100 times more expensive than industrial pure Al (2N) and the high cost of high purity Al is a barrier for commercial application. Doche et al. investigated and compared the polarization characteristics of

Received: November 17, 2020
Revised: January 9, 2021
Published: January 26, 2021

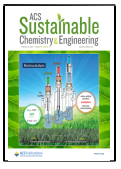

https://dx.doi.org/10.1021/acssuschemeng.0c08415
ACS Sustainable Chem. Eng. 2021, 9, 2300−2308

Table 1. Elemental Compositions of Pure Aluminum with Different Grades (wt/ppm)

sample	Mg	Si	V	Mn	Fe	Ni	Cu	Zn	Ga	Al
2N8	10.4	168.7	322.5	7.2	670.5	32.1	1.1	170.6	148.8	bal
3N6	1.2	52.9	2.8	4.7	144.4	10.8	0.9	78.0	76.7	bal
3N8	15.7	8.3	<0.1	<0.05	18.4	0.7	37.9	0.3	0.3	bal
4N6	3.9	13.6	0.2	<0.1	2.8	0.1	4.5	1.7	0.2	bal
5N	2.3	2.2	<0.1	<0.1	2.0	<0.1	1.6	0.2	<0.05	bal

3N5 and 5N pure Al anodes in a 4 M NaOH electrolyte, and the 3N5 Al anode exhibited a similar polarization but suffered from a higher corrosion rate compared with 5N Al.[23] Recently, Cho et al. compared the battery performance of 2N5 and 4N Al anodes, and the battery performance with 2N5 Al was lower than that with 4N Al on standby and discharge status due to the impurity-induced complex layer.[24] These studies to some extent help us to understand the effect of impurity on electrochemical performance of pure Al. However, the previous studies only investigate two types of pure Al anodes, and it is necessary to systematically study pure Al anodes with more different purities. Meanwhile, the previous studies mainly evaluated the effect of impurity elements (Fe, Si, Cu, etc.),[23−27] but the effects of the active alloying elements on electrochemical and battery performance are rarely discussed. Additionally, the relationship between battery performance and microstructure change of Al anodes caused by impurities is also neglected.

In this study, the electrochemical and discharge performance of Al anodes with five different grades (2N8, 3N6, 3N8, 4N6, and 5N) is systematically investigated, and the contents of impurities and the associated microstructure change are discussed in detail. The aim of this study is to clarify how impurities in a pure Al anode affect the battery performance.

EXPERIMENTAL SECTION

Self-Corrosion Evaluation. Pure Al specimens (Nantong Taide Electronic Material Technology Co. Ltd.) with a size of 10 × 10 × 10 mm^3 were polished with silicon carbide sandpaper from 240 to 2000 grit and cleaned with ethanol and then immersed in a 4 mol L^{-1} KOH solution for 60 min. The weight of each specimen was measured by a high sensitivity balance (0.01 mg resolution) before and after immersion. After immersion, the corrosion products on the aluminum surface were removed by immersing in a solution containing 2 wt % CrO_3 and 5 wt % H_3PO_4 at 80 °C for ∼5 min.[28] The corrosion rate was calculated using eq 1

$$\text{corrosion rate} = \frac{\text{weight loss}}{\text{surface area} \times \text{immersion time}} \quad (\text{mg}\cdot\text{min}^{-1}\cdot\text{cm}^{-2}) \tag{1}$$

Electrochemical Measurements. The specimens were prepared from commercial 2N8 Al, 3N6 Al, 3N8 Al, 4N6 Al, and 5N Al. The Al anodes were machined and insulated with epoxy resin to expose only a working surface of 10 × 10 mm^2. Before testing, the working surface was polished with the silicon carbide sandpaper from 240 to 2000 grit followed by ultrasonic cleaning in water and ethanol in turn. The open-circuit potential (OCP) and Tafel polarization were carried out in a 4 M KOH solution with a standard three-electrode configuration in a potentiostat (CHI 660E) at 25 °C. The mercury/mercury oxide electrode (Hg/HgO) was selected as the reference electrode, while a platinum sheet (25 × 25 mm^2) was used as the counter electrode. The OCP measurement was performed for 1 h, while the potentiodynamic polarization was measured at a scan rate of 1 mV s^{-1}. Electrochemical impedance spectroscopy (EIS) was carried out at an open-circuit potential with a 5 mV sine perturbation from 100 kHz to 0.1 Hz with Gamry potentiostat (Gamry Ref 600). All electrochemical tests were repeated more than three times.

Materials Characterizations. Elemental analysis of the various pure Al samples was conducted by an inductively coupled plasma optical emission spectrometer (iCAP 7600, Thermo Scientific). Morphologies of the specimens before and after immersion were characterized by a scanning electron microscope (TESTAN MIRA3 and VEGA3) equipped with an energy dispersion spectrum detector. SKPFM (scanning Kelvin probe force microscopy) measurement was conducted to acquire the Volta potential mappings using a Dimension FastScan Bio atomic force microscope (Bruker). The dual-scan mode was carried out for the acquisition of accurate surface potential mapping. Topography data were recorded at the first scan. In the second step for Volta potential mapping, a lift scan height of 100 nm was needed to avoid the topography impact on the Volta potential mapping. All mappings were acquired in air at ambient temperature under the controlled relative humidity. The specimen with a size of 10 × 10 mm^2 for SKPFM measurement was wet-ground with SiC paper of up to 2000 grit and then mechanically polished using a monocrystalline diamond paste to remove the polishing scratch. Finally, specimens were ultrasonically cleaned with acetone, alcohol, and deionized water in sequence and then dried under vacuum before testing.

Battery Testing. The Al-air batteries were housemade (Figure S1). The anodes were the pure Al specimens with different purities, while the cathodes were self-prepared air electrodes decorated with a modified MnO_2 catalyst, which were prepared following the previous research (details are in the Supporting Information).[29] The as-fabricated Al-air batteries were galvanostatically discharged at 20, 60, and 100 mA cm^{-2} using a battery discharge system (LAND, CT2001A) at 25 °C. The weight before and after discharge was measured to calculate the discharge efficiency. The anode utilization and specific capacity were calculated using the following equations (eqs 2 and 3)

$$\text{anode utilization} = \frac{9It}{mF} \times 100\% \tag{2}$$

$$\text{specific capacity} = \frac{It}{3.6m} \tag{3}$$

where I is the current (A), m is the weight loss (g) during the discharge time, F is the Faraday constant, and t is the discharge time (s).

RESULTS AND DISCUSSION

Microstructure and Self-Corrosion Analysis. The elemental compositions of the various pure Al anodes obtained by inductively coupled plasma optical emission spectrometry (ICP-OES) are shown in Table 1. The 2N8, 3N6, 3N8, 4N6, and 5N Al anodes representing the content of Al are 99.8, 99.96, 99.98, 99.996, and 99.999%, respectively, and the purity corresponds to the content of the Al element. With the increase in purity, the total content of impurities gradually decreases. The main impurity elements in 2N8 Al are Fe, V, Zn, Si, and Ga, while the main impurity elements in 3N6 Al are Fe, Ga, and Zn. There is a significant increase of Cu in 3N8 Al, and there are less impurities in 4N6 Al and 5N Al. It is considered that the impurity elements can drastically affect the

https://dx.doi.org/10.1021/acssuschemeng.0c08415
ACS Sustainable Chem. Eng. 2021, 9, 2300−2308

self-corrosion behavior and electrochemical performance of pure Al anodes.

Figure 1 shows the scanning electron microscopy (SEM) images of pure Al anodes with various purities. The SEM

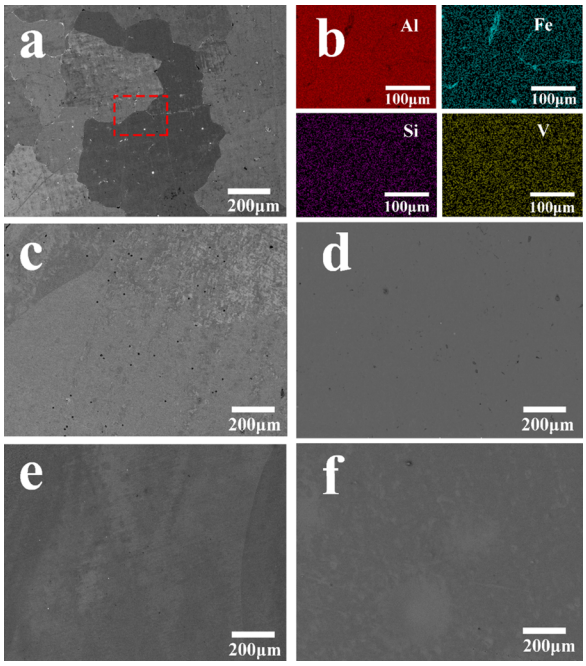

Figure 1. SEM images of (a) 2N8, (c) 3N6, (d) 3N8, (e) 4N6, and (f) 5N Al anodes and (b) elemental mappings of 2N8 Al.

image of 2N8 Al displays that there are a lot of precipitates at the grain boundaries caused by the high content of impurities (Figure 1a). The energy-dispersive spectroscopy (EDS) mappings show that the precipitate is mainly an Fe-rich phase, and the Fe-rich precipitates with an uneven microstructure can act as corrosion centers to accelerate the corrosion. With the increase in purity, there are almost no precipitates in 3N6, 3N8, 4N6, and 5N Al, and also, there are less and less porosities or holes in the Al anodes.

Table 2 shows the self-corrosion rates of the Al anodes evaluated by weight loss and hydrogen evolution in a 4 M KOH solution at room temperature. As illustrated, the self-corrosion and hydrogen evolution rates are highly related to the purity of the Al anode with the following order: 2N8 > 3N6 > 3N8 > 4N6 > 5N. The decrease in self-corrosion rate is explained by the decrease of negative impurity elements, especially Fe and Si.[30] The 2N8 Al anode displays the largest self-corrosion rate (0.519 mg·min^{-1}·cm^{-2}) due to the highest impurity content, while the corrosion rate of 5N Al (0.057 mg·min^{-1}·cm^{-2}) is the smallest. The self-corrosion rate of the 3N6 Al anode (0.246 mg·min^{-1}·cm^{-2}) is significantly smaller than that of the 2N8 Al anode. Meanwhile, the 3N6, 3N8, and 4N6 Al anodes show similar self-corrosion rates, meaning that the increase in purity from 3N6 to 4N6 Al does not significantly affect the self-corrosion rate.

Table 2. Self-Corrosion Rates of the Various Pure Al Anodes in 4 M KOH

aluminum	weight loss (mg)	rate of weight loss (mg·min^{-1}·cm^{-2})	rate of hydrogen evolution (mg·min^{-1}·cm^{-2})
2N8	31.14	0.519	0.820
3N6	14.76	0.246	0.446
3N8	12.12	0.202	0.379
4N6	10.86	0.181	0.321
5N	3.42	0.057	0.107

The SEM images of the Al anodes after immersion are shown in Figure 2. The surface of 2N8 Al shows non-uniform corrosion morphology with a large amount of very deep corrosion pits, demonstrating the most severe corrosion damage. Noticeably, the surface of 2N8 Al contains two significantly different corrosion morphology features: deeper and larger "short strip" corrosion pits and many small corrosion pits. The length of the short strip etch pit is 0.5−2 mm, which might be due to the superposition of the adjacent pits. The small etch pits with diameters ranging from tens of micrometers to several millimeters are densely distributed. The EDS result shows that the particles near the etch pits are iron-rich phases (Figure 3 and Table 3), and these iron-rich phases with low hydrogen evolution overpotentials can accelerate the self-corrosion rate. The 3N6, 3N8, 4N6, and 5N Al anodes after corrosion show smaller and shallower corrosion pits with relatively uniform distribution, and no large pits are noticed. EDS of 3N6 Al shows that the contents of Ga, Zn, and Fe in corrosion pits and the inclusions are much higher than those in the matrix (Table 3). The enrichment of Ga is ascribed to the activation process via dissolution and redeposition, which is helpful to improve the electrochemical activity.[5] Particularly, the 5N Al anode displays a fairly smooth surface with the

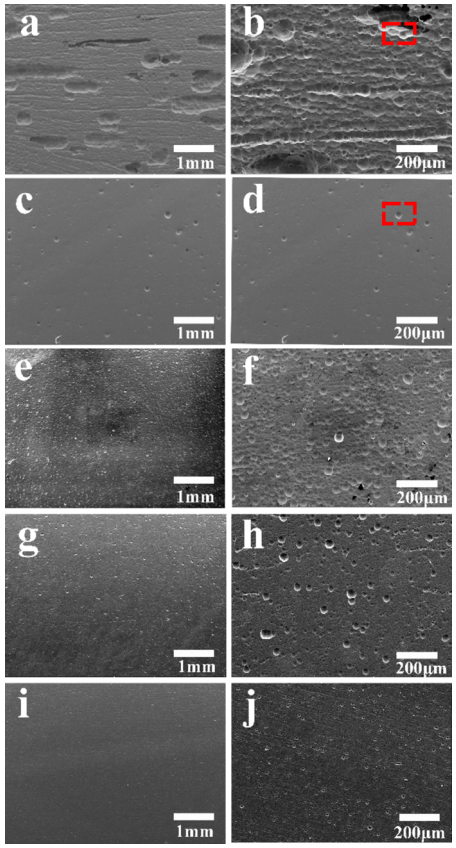

Figure 2. SEM images of (a, b) 2N8 Al, (c, d) 3N6 Al, (e, f) 3N8 Al, (g, h) 4N6 Al, and (i, j) 5N Al after immersion in 4 M KOH for 60 min.

https://dx.doi.org/10.1021/acssuschemeng.0c08415
ACS Sustainable Chem. Eng. 2021, 9, 2300−2308

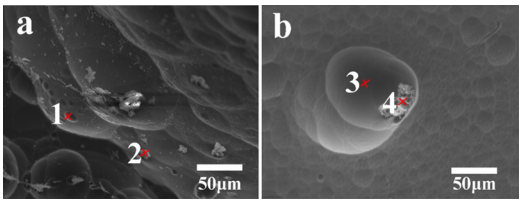

Figure 3. SEM images of the marked corrosion pits in Figure 2 for (a) 2N8 Al and (b) 3N6 Al.

Table 3. Elemental Compositions of the Labeled Regions in Figure 3

	elements wt %				
region	Al	Fe	Ga	Zn	Ni
1	83.85	0.39	4.31	11.45	
2	20.04	65.87	2.57	8.48	3.04
3	99.79	0.06	0.18	0.03	
4	65.25	32.27	0.39	2.08	

smallest corrosion pits. Overall, the corrosion morphology agrees well with the self-corrosion rate results (Table 2).

To further evaluate the influence of impurity on the self-corrosion rate of Al anodes, the surface potential maps of Al anodes using atomic force microscopy (AFM)/SKPFM are shown in Figure 4. The 2N8 Al anode shows an uneven

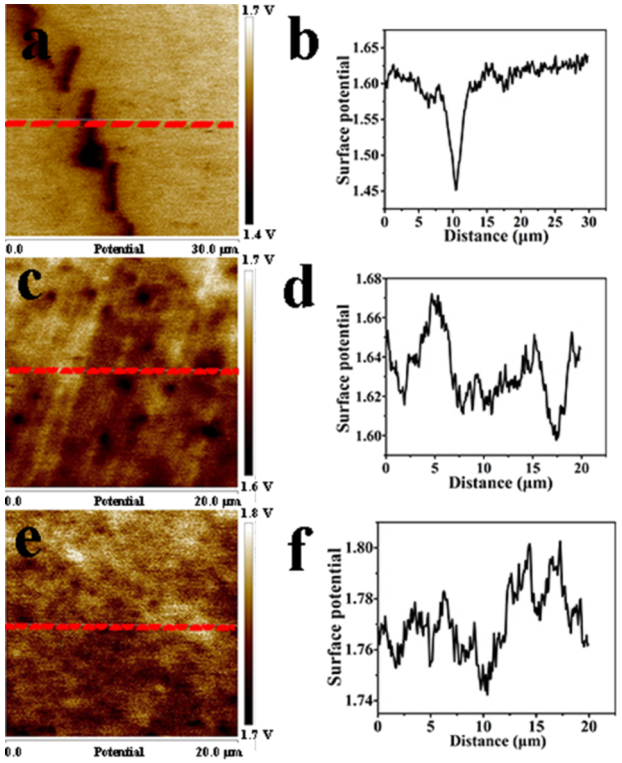

Figure 4. SKPFM images and Volta potential difference profile of (a, b) 2N8 Al, (c, d) 3N6 Al, and (e, f) 5N Al.

distribution of surface potential, and the precipitate has the largest potential difference (ΔE = 150 mV) across the matrix. The galvanic interactions between the intermetallic particles within the Al matrix can form galvanic cells to accelerate the self-corrosion rate.[31,32] With the increase in purity, the surface potential becomes relatively uniform with smaller difference. The 5N Al anode shows the smallest surface potential difference (ΔE = 30 mV). The small surface potential difference can alleviate the self-corrosion rate.

It is deduced that the significant difference in the self-corrosion rate of the Al anodes is ascribed to various impurities. The main impurities in 2N8 Al are Fe, V, and Si. Fe tends to precipitate at grain boundaries to cause large surface potential difference within the matrix, which can lead to galvanic corrosion and accelerate the self-corrosion of Al. Meanwhile, iron-rich phases have a relatively low hydrogen evolution overpotential, which also facilitates hydrogen evolution.[30,33] Therefore, the 2N8 Al anode with the highest impurity demonstrates the largest self-corrosion rate and the roughest corrosion morphology. The 3N6 Al anode also has a high iron content but little precipitates. Thus, the 3N6 Al anode shows a much smaller self-corrosion rate than the 2N8 Al anode. The 3N8 Al anode has a higher copper content than the 4N Al anode, and the copper impurity also has a low hydrogen evolution overpotential.[34] Meanwhile, the total content of Zn and Ga in the 3N8 anode is lower, and the total content of Fe and Si is similar. Therefore, the 4N6 Al anode shows a smaller self-corrosion rate and flatter corrosion surface. The 5N Al anode exhibits the lowest self-corrosion rate and the smallest amount of corrosion pits.

Electrochemical Performance. Figure 5 presents the open-circuit potential (OCP) curves and Tafel plots of the various Al anodes. Each open-circuit potential curve shows a relatively stable potential, and the OCP values of all Al anodes are shown in Table 4. The 2N8 Al anode displays the most positive open-circuit potential, while the 5N Al anode displays the most negative potential. Namely, the open-circuit potential negatively shifts along with the increase in purity, except the 3N6 Al anode. It is reported that the accumulation of surface hydrides and impurities (such as Fe, Si, and Cu) on the Al surface is the key factor to shift the open-circuit potential.[35,36] Accordingly, the 5N Al anode displays the most negative open-circuit potential due to the minimum accumulation of corrosion products. The open-circuit potential of 3N6 Al is more negative than that of 3N8 Al or 4N6 Al. This may be related to Ga and Zn in the 3N6 Al anode, which can help to lower the aluminum anodic polarization and negatively shift the electrode potential.[37,38] Therefore, the open-circuit potential of the Al anode is not only related to the purity of Al but also related to the type and content of some specific impurity elements.

The Tafel plots and corresponding corrosion parameters of the various Al anodes are shown in Figure 5b and Table 4. E_{corr} here reflects the electrochemical activity of anodic dissolution,[39,40] and the more negative E_{corr} of the pure Al anode signifies better electrochemical activity. The E_{corr} of the Al anode is close to the respective open-circuit potential, and the E_{corr} shifts negatively with the increase in purity, except the 3N6 Al anode. It is deduced that the 5N Al anode shows the highest electrochemical activity. The self-corrosion current density (I_{corr}) is also related to the content of the cathodic phase elements in the Al anode. The 5N Al anode displays the smallest self-corrosion current density, while the 2N Al anode displays the largest self-corrosion current density, which are consistent with the weight loss results in Table 2. The 3N6 Al anode shows a more negative corrosion potential than the 3N8 Al or 4N6 Al anode due to the Ga and Zn elements. The Zn element can increase the hydrogen evolution overpotential,[37] and the Ga element is beneficial for activation.[41] However, the

https://dx.doi.org/10.1021/acssuschemeng.0c08415
ACS Sustainable Chem. Eng. 2021, 9, 2300−2308

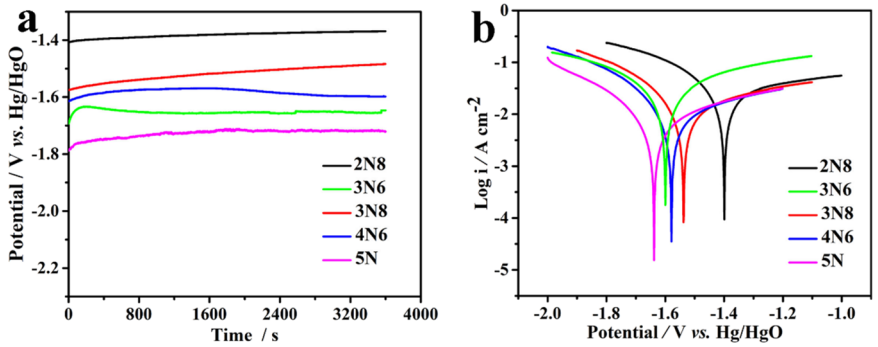

Figure 5. (a) Open-circuit potential curves and (b) Tafel plots of the Al anodes with various purities.

Table 4. Open-Circuit Potentials, Self-Corrosion Potentials, and Self-Corrosion Current Densities of the Various Al Anodes

	2N8	3N6	3N8	4N6	5N
OCP (V vs Hg/HgO)	−1.382	−1.653	−1.518	−1.583	−1.728
E_{corr} (V vs Hg/HgO)	−1.399	−1.598	−1.538	−1.579	−1.638
I_{corr} (mA cm^{-2})	57.27	23.93	22.51	16.76	11.40

relatively high total content of cathodic phase elements still contributes to a higher corrosion current density of the 3N6 Al anode.

Electrochemical impedance spectroscopy was also used to characterize the various pure Al anodes at an open-circuit potential. Figure 6a shows the obtained Nyquist plots, which

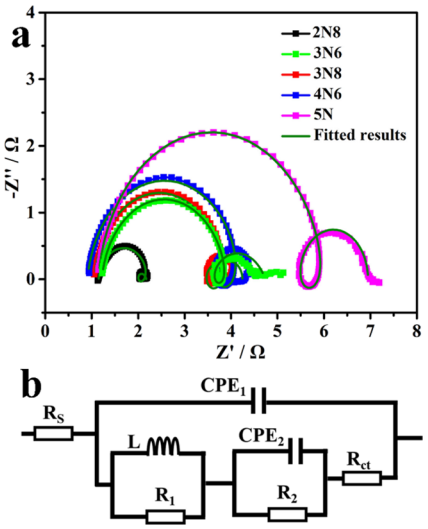

Figure 6. (a) Nyquist plots of the various Al anodes and (b) equivalent circuit for EIS.

are fitted using the equivalent circuit in Figure 6b, where R_s represents the solution resistance, R_{ct} is the charge-transfer resistance, CPE_1 and CPE_2 are constant phase elements, and R_1 and R_2 are resistances corresponding to the inductive arc at the medium frequency region and the capacitive arc at the low frequency region, respectively. All plots are composed of two capacitive semicircles at high and low frequency regions and an induction arc at the intermediate frequency region. All the Nyquist plots show similar shapes, indicating the same reaction mechanism for the Al anodes with various purities. The loop at high frequency is related to the Al dissolution reaction ($Al \rightarrow Al^{3+}$),[42] while the loop at low frequency is related to the surface film growth reaction ($Al^{3+} + 3OH^- \rightarrow Al(OH)_3$).[43] The inductive loop corresponds to the relaxation and adsorption of OH^- on the electrode surface ($Al(OH)_3 \leftrightarrow Al(OH)_4^-$). The diameter of the loop at high frequency reflects the charge-transfer resistance (R_{ct} in the equivalent circuit) of Al dissolution associated with hydrogen evolution. Table 5 lists the extracted parameter values of the fitted Nyquist plots via Gamry Echem Analyst. The chi-squared (χ^2) values in Table 5 indicate the good suitability of the model and precision of the fitted data. R_{ct} values for the 2N8, 3N6, 3N8, 4N6, and 5N Al anodes are 1.13, 2.18, 2.33, 2.79, and 4.28 Ω, respectively. A small charge-transfer resistance is beneficial to the dissolution process. The polarization resistance (R_p) values calculated by the sum of R_{ct}, R_1, and R_2 for the 2N8, 3N6, 3N8, 4N6, and 5N Al anodes are 1.35, 2.8, 3.29, 3.85, and 6.39 Ω, respectively. The R_{ct} and R_p increase with the increase in purity. The larger the R_p, the smaller the self-corrosion rate. Therefore, the Al anode with a higher purity displays a larger corrosion resistance. This is consistent with the trend of weight loss (Table 2) and Tafel plot results (Table 4).

Battery Performance. Figure 7a shows the open-circuit voltage (OCV) and galvanostatic discharge curves of the assembled Al-air batteries with the various Al anodes. The Al-air battery with the 5N Al anode displays the highest working voltage, and the Al-air battery with the 3N6 Al anode displays the second largest open-circuit voltage due to a large amount of active elements inside. The open-circuit voltages of the Al-air batteries with 2N8 and 3N8 Al anodes are lower than those with 4N Al or 5N Al owing to a high content of impurities. The OCV of the Al-air batteries with various Al anodes compared with those reported in literature is shown and discussed in Table S1. Figure 7b–d shows the discharge curves of the Al-air batteries at various current densities of 20, 60, and 100 mA cm^{-2}, respectively. At a low current density of 20 mA cm^{-2}, the order of discharge voltage is as follows: 5N > 3N6 > 4N6 > 3N8 > 2N8. The anode electrochemical activity plays a key role in achieving a high discharge voltage. The Al-air battery with 5N Al maintains a stable and high discharge voltage, which explains that the smallest content of impurity and the highest corrosion resistance lead to less accumulation of corrosion products. The second highest discharge voltage of the Al-air battery with 3N6 Al is related to Ga and Zn active elements, which can shield the active cathodic sites on the anode surface and increase the contact area between the anode and electrolyte through a dissolution and deposition process. As explained, the Al anode with a low purity possesses smaller

https://dx.doi.org/10.1021/acssuschemeng.0c08415
ACS Sustainable Chem. Eng. 2021, 9, 2300−2308

Table 5. Fitted Parameter Values from the Nyquist Plots

	2N8	3N6	3N8	4N6	5N
R_s (Ω)	1.147	1.221	1.067	0.911	1.143
CPE_1 (Fcm^{-2})	6.88×10^{-4}	1.19×10^{-5}	2.30×10^{-5}	2.59×10^{-5}	2.11×10^{-5}
a_1	0.88	0.93	0.96	0.93	0.94
L (H)	4.84×10^{-3}	7.17×10^{-4}	1.17×10^{-3}	4.56×10^{-4}	1.62×10^{-3}
R_1 (Ω)	0.32	0.39	0.45	0.52	0.59
CPE_2 (Fcm^{-2})	12.48×10^{-2}	4.46×10^{-2}	6.07×10^{-2}	7.03×10^{-2}	4.73×10^{-2}
a_2	1	0.73	1	1	1
R_2 (Ω)	0.18	0.23	0.51	0.54	1.52
R_{ct} (Ω)	0.85	2.18	2.33	2.79	4.28
R_p (Ω)	1.35	2.8	3.29	3.85	6.39
goodness of fit	1.64×10^{-4}	5.73×10^{-4}	8.24×10^{-4}	9.27×10^{-4}	1.21×10^{-4}

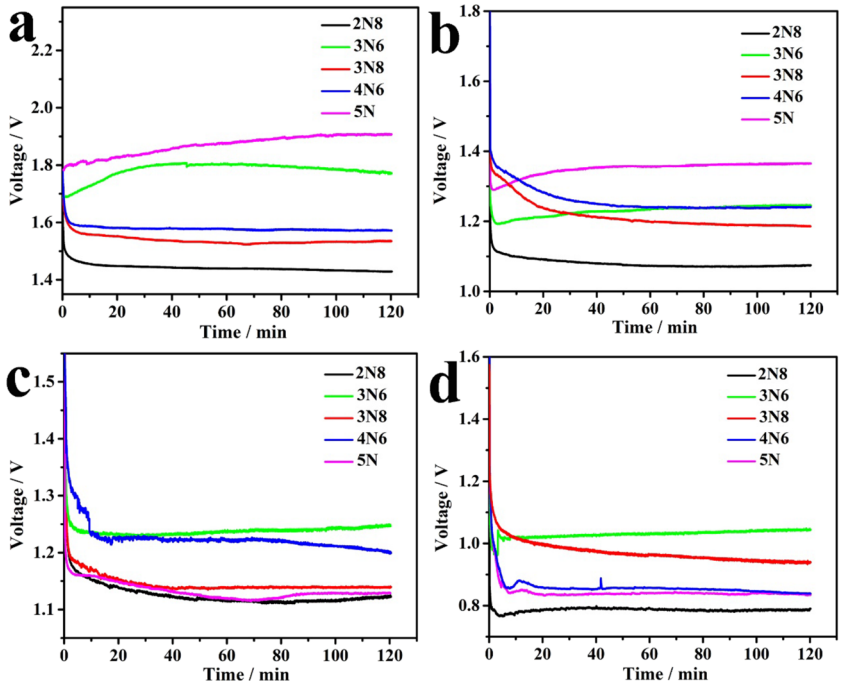

Figure 7. Discharge curves of the various Al-air batteries at (a) open-circuit status and current densities of (b) 20, (c) 60, and (d) 100 mA cm^{-2}.

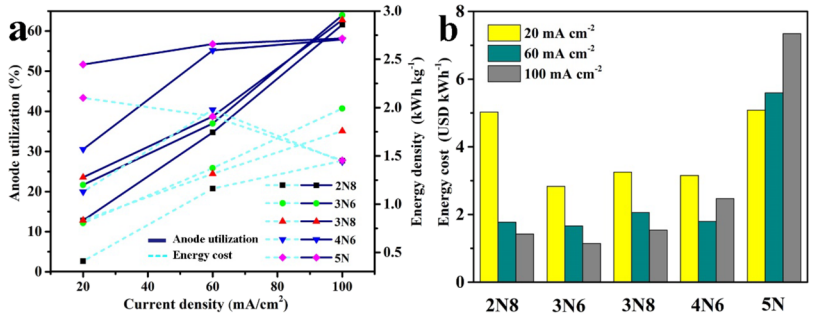

Figure 8. (a) Anode utilization and energy density as a function of current density and (b) energy cost of various Al anodes for Al-air batteries.

charge-transfer and polarization resistances, leading to a low resistance of the full cell. Hence, the Al-air battery with the 2N8, 3N6, or 3N8 Al anode shows a higher discharge voltage when the discharge current density reaches up to 60 mA cm^{-2}. The voltage difference of the Al-air batteries becomes smaller at a high current density. When the discharge current densities are 60 and 100 mA cm^{-2}, the voltages of all Al-air batteries display a sharp voltage drop, which is explained by the formed passive film on the Al surface to increase the resistance. The voltage of the Al-air battery with the 3N6 Al anode gradually increases along discharging and keeps the highest discharge voltage. The Al-air battery with 5N Al shows a relatively low discharge voltage similar to that with 2N8 Al.

Figure 8a displays the anodic utilization and energy density of the Al-air batteries at different discharge current densities, and the results are listed in Table 6. The specific capacity of the Al anode gradually increases with the increase in current density. Both the discharge reaction and self-corrosion reaction

https://dx.doi.org/10.1021/acssuschemeng.0c08415
ACS Sustainable Chem. Eng. 2021, 9, 2300−2308

Table 6. Discharge Performance of the Al-Air Batteries at Different Current Densities

anodes	current density (mA cm^{-2})	anode utilization	power density (mW cm^{-2})	energy density (kWh kg^{-1})
2N8	20	12.79%	21.49	0.40
	60	34.74%	67.36	1.16
	100	61.62%	79.02	1.45
3N6	20	21.67%	24.93	0.80
	60	36.97%	74.89	1.37
	100	63.96%	104.54	1.99
3N8	20	23.57%	23.39	0.83
	60	38.75%	68.29	1.32
	100	62.77%	91.11	1.76
4N6	20	30.53%	24.82	1.13
	60	55.20%	72.65	1.98
	100	57.90%	84.16	1.44
5N	20	51.66%	27.29	2.10
	60	56.76%	67.76	1.91
	100	58.16%	83.46	1.45

consume the Al anode. When the self-corrosion reaction is suppressed, the Al anode is mainly consumed by the discharge reaction, achieving high anode efficiency. Moreover, when the applied current density exceeds 60 mA cm^{-2}, the specific capacities of the 3N6, 3N8, and 4N6 Al anodes increase significantly. The 5N Al anode shows the largest specific capacity and the highest anode utilization at current densities of 20 and 60 mA cm^{-2}. However, the 3N6, 3N8, and 4N6 Al anodes show higher anode utilization at a higher current density of 100 mA cm^{-2}. The specific capacities of 3N6, 3N8, and 4N6 Al anodes are 1836, 1906, and 1870 Ah kg^{-1}, respectively. The energy density and power density were also calculated. The energy density of the Al anode with a high purity (4N6 and 5N) decreases with the increase in current density. The energy density of the Al anode with a low purity (2N8, 3N6, and 3N8) gradually increases with the increase in current density. The power densities of all the Al anodes increase with the increase in current density. The 5N Al anode displays the largest power density at a low current density of 20 mA cm^{-2}, while the 3N6 Al anode displays the largest power density at a high current density of 100 mA cm^{-2}.

To understand the cost-effectiveness of the various Al anodes, a rough cost evaluation is analyzed following eq 4

$$\text{energy cost} = \frac{\text{unit price}}{\text{energy density}} \ (\text{USD kWh}^{-1}) \tag{4}$$

The prices of 2N8, 3N6, 3N8, 4N6, and 5N Al quoted by a local supplier (Nantong Taide Electronic Material Technology Co. Ltd.) are 2.07, 2.28, 2.71, 3.56, and 10.68 USD per kilogram, respectively, and the corresponding energy cost is shown in Figure 8b. The Al anodes with low and high purities demonstrate higher energy cost. The energy cost of 5N Al is higher than the others as the cost of 5N Al is the highest. Meanwhile, the energy cost of 2N8 Al is also quite high due to the low utilization rate. Interestingly, the 3N6 Al anode displays the lowest energy cost at all the discharge current densities. Although this is a very rough cost evaluation, it is demonstrated that the 3N6 Al anode is the best cost-effective choice among all the pure Al anodes for Al-air batteries by comprehensive consideration of battery performance and cost.

CONCLUSIONS

Five kinds of pure Al anodes have been studied to evaluate the effect of impurities on electrochemical and battery performance, where the contents of impurities and the associated microstructure change are discussed in detail. With the increase in purity of aluminum, impurities such as Fe and Si are less. When the purity of Al is above 99.9%, the impurity enrichments disappear in the microstructure, which is beneficial to suppress the self-corrosion reaction so as to achieve high anode efficiency. The Al-air battery with the 5N Al anode displays the largest discharge voltage and anode efficiency at 20 mA cm^{-2}. The Al-air battery with 3N6 Al shows a larger discharge voltage and higher anode efficiency than that with 4N6 Al at 100 mA cm^{-2}. The 3N6 Al anode has been demonstrated as the best cost-effective choice for Al-air batteries.

ASSOCIATED CONTENT

Supporting Information

The Supporting Information is available free of charge at https://pubs.acs.org/doi/10.1021/acssuschemeng.0c08415.

Details of the preparation of the air cathode, the scheme and a real picture of the housemade Al-air battery, and comparison of open-circuit voltages of the Al-air batteries with various Al anodes (PDF)

AUTHOR INFORMATION

Corresponding Authors

Chaopeng Fu − *School of Materials Science and Engineering, Shanghai Jiao Tong University, Shanghai 200240, P. R. China*; orcid.org/0000-0001-9896-9538; Email: chaopengfu@sjtu.edu.cn

Anping Dong − *School of Materials Science and Engineering, Shanghai Jiao Tong University, Shanghai 200240, P. R. China*; Email: apdong@sjtu.edu.cn

Authors

Jianming Ren − *School of Materials Science and Engineering, Shanghai Jiao Tong University, Shanghai 200240, P. R. China*

Qing Dong − *School of Materials Science and Engineering, Shanghai Jiao Tong University, Shanghai 200240, P. R. China*

Min Jiang − *School of Materials Science and Engineering, Shanghai Jiao Tong University, Shanghai 200240, P. R. China*

Guoliang Zhu − *School of Materials Science and Engineering, Shanghai Jiao Tong University, Shanghai 200240, P. R. China*

Jiao Zhang − *School of Materials Science and Engineering, Shanghai Jiao Tong University, Shanghai 200240, P. R. China*

Baode Sun − *School of Materials Science and Engineering, Shanghai Jiao Tong University, Shanghai 200240, P. R. China*

Complete contact information is available at: https://pubs.acs.org/10.1021/acssuschemeng.0c08415

Notes

The authors declare no competing financial interest.

https://dx.doi.org/10.1021/acssuschemeng.0c08415
ACS Sustainable Chem. Eng. 2021, 9, 2300−2308

■ ACKNOWLEDGMENTS

This work was supported by National Natural Science Foundation of China (grant no.: 51874197, 51704106, and 51704195).

■ LIST OF SYMBOLS

2N8, 3N6, 3N8, 4N6, and 5N grade of pure aluminum (contents of aluminum are 99.8, 99.96, 99.98, 99.996, and 99.999 wt %, respectively)
NHE normal hydrogen electrode
OCP open-circuit potential
OCV open-circuit voltage
CPE constant phase element
EIS electrochemical impedance spectroscopy
M molar/mol L^{-1}

■ REFERENCES

(1) Ryu, J.; Park, M.; Cho, J. Advanced Technologies for High-Energy Aluminum−Air Batteries. *Adv. Mater.* **2019**, *31*, 1804784−1804791.
(2) Ma, J.; Li, W.; Wang, G.; Li, Y.; Ren, F.; Xiong, Y. Influences of L-Cysteine/Zinc Oxide Additive on the Electrochemical Behavior of Pure Aluminum in Alkaline Solution. *J. Electrochem. Soc.* **2018**, *165*, A266−A272.
(3) Hopkins, B. J.; Shao-Horn, Y.; Hart, D. P. Suppressing corrosion in primary aluminum−air batteries via oil displacement. *Science* **2018**, *362*, 658−661.
(4) Xiang, F.; Chen, X.; Yu, J.; Ma, W.; Li, Y.; Yang, N. Synthesis of three-dimensionally ordered porous perovskite type $LaMnO_3$ for Al-air battery. *J. Mater. Sci. Technol.* **2018**, *34*, 1532−1537.
(5) Egan, D. R.; Ponce de León, C.; Wood, R. J. K.; Jones, R. L.; Stokes, K. R.; Walsh, F. C. Developments in electrode materials and electrolytes for aluminium−air batteries. *J. Power Sources* **2013**, *236*, 293−310.
(6) Liu, J.; Wang, D.; Zhang, D.; Gao, L.; Lin, T. Synergistic effects of carboxymethyl cellulose and ZnO as alkaline electrolyte additives for aluminium anodes with a view towards Al-air batteries. *J. Power Sources* **2016**, *335*, 1−11.
(7) Pino, M.; Herranz, D.; Chacón, J.; Fatás, E.; Ocón, P. Carbon treated commercial aluminium alloys as anodes for aluminium-air batteries in sodium chloride electrolyte. *J. Power Sources* **2016**, *326*, 296−302.
(8) Fan, L.; Lu, H.; Leng, J. Performance of fine structured aluminum anodes in neutral and alkaline electrolytes for Al-air batteries. *Electrochim. Acta* **2015**, *165*, 22−28.
(9) Fan, L.; Lu, H. The effect of grain size on aluminum anodes for Al−air batteries in alkaline electrolytes. *J. Power Sources* **2015**, *284*, 409−415.
(10) Ma, J.; Wen, J.; Gao, J.; Li, Q. Performance of Al−1Mg−1Zn−0.1Ga−0.1Sn as anode for Al-air battery. *Electrochim. Acta* **2014**, *129*, 69−75.
(11) Eftekhari, A.; Corrochano, P. Electrochemical energy storage by aluminum as a lightweight and cheap anode/charge carrier. *Sustainable Energy Fuels* **2017**, *1*, 1246−1264.
(12) Moghanni-Bavil-Olyaei, H.; Arjomandi, J. Enhanced electrochemical performance of Al−0.9Mg−1Zn−0.1Mn−0.05Bi−0.02In fabricated from commercially pure aluminum for use as the anode of alkaline batteries. *RSC Adv.* **2016**, *6*, 28055−28062.
(13) Sun, Z.; Lu, H.; Fan, L.; Hong, Q.; Leng, J.; Chen, C. Performance of Al-Air Batteries Based on Al−Ga, Al−In and Al−Sn Alloy Electrodes. *J. Electrochem. Soc.* **2015**, *162*, A2116−A2122.
(14) Xiong, H.; Yin, X.; Yan, Y.; Dai, Y.; Fan, S.; Qiao, X.; Yu, K. Corrosion and Discharge Behaviors of Al-Mg-Sn-Ga-In in Different Solutions. *J. Mater. Eng. Perform.* **2016**, *25*, 3456−3464.
(15) Li, Q.; Bjerrum, N. J. Aluminum as anode for energy storage and conversion: a review. *J. Power Sources* **2002**, *110*, 1−10.
(16) Wang, H. Z.; Leung, D. Y. C.; Leung, M. K. H.; Ni, M. A review on hydrogen production using aluminum and aluminum alloys. *Renewable Sustainable Energy Rev.* **2009**, *13*, 845−853.
(17) Liu, X.; Zhang, P.; Xue, J. The role of micro-naoscale AlSb precipitates in improving the discharge performance of Al-Sb alloy anodes for Al-air batteries. *J. Power Sources* **2019**, *425*, 186−194.
(18) Wu, Z.; Zhang, H.; Guo, C.; Zou, J.; Qin, K.; Ban, C.; Nagaumi, H. Effects of indium, gallium, or bismuth additions on the discharge behavior of Al-Mg-Sn-based alloy for Al-air battery anodes in NaOH electrolytes. *J. Solid State Electrochem.* **2019**, *23*, 2483−2491.
(19) Ren, J.; Ma, J.; Zhang, J.; Fu, C.; Sun, B. Electrochemical performance of pure Al, Al−Sn, Al−Mg and Al−Mg−Sn anodes for Al-air batteries. *J. Alloys Compd.* **2019**, *808*, 151708−151714.
(20) Yu, Y.; Chen, M.; Wang, S.; Hill, C.; Joshi, P.; Kuruganti, T.; Hu, A. Laser sintering of printed anodes for al-air batteries. *J. Electrochem. Soc.* **2018**, *165*, A584−A592.
(21) Wu, Z.; Zhang, H.; Zou, J.; Shen, X.; Qin, K.; Ban, C.; Cui, J.; Nagaumi, H. Enhancement of the discharge performance of Al-0.5Mg-0.1Sn-0.05Ga (wt.%) anode for Al-air battery by directional solidification technique and subsequent rolling process. *J. Alloys Compd.* **2020**, *827*, 154272−154281.
(22) Zheng, X.; Zhang, T.; Yang, H.; Zheng, Q.; Gao, Y.; Liu, Z.; Wang, W.; Wang, K. Friction stir processing induced elctrochemical performance improvement of commercial Al for Al-air battery. *Electrochim. Acta* **2020**, *354*, 136635−136644.
(23) Doche, M. L.; Novel-Cattin, F.; Durand, R.; Rameau, J. J. Characterization of different grades of aluminum anodes for aluminum/air batteries. *J. Power Sources* **1997**, *65*, 197−205.
(24) Cho, Y.-J.; Park, I.-J.; Lee, H.-J.; Kim, J.-G. Aluminum anode for aluminum−air battery − Part I: Influence of aluminum purity. *J. Power Sources* **2015**, *277*, 370−378.
(25) Roald, B.; Streicher, M. A. Corrosion Rate and ETCH Structures of Aluminum; Effect of Heat Treatment and Impurities. *J. Electrochem. Soc.* **1950**, *97*, 283.
(26) Streicher, M. A. The dissolution of aluminum in sodium hydroxide solutions. II. *J. Electrochem. Soc.* **1949**, *96*, 170−194.
(27) Streicher, M. A. The dissolution of aluminum in sodium hydroxide solutions. *J. Electrochem. Soc.* **1948**, *93*, 285−316.
(28) Jingling, M.; Fengzhang, R.; Guangxin, W.; Yi, X.; Yaqiong, L.; Jiuba, W. Electrochemical performance of melt-spinning Al−Mg−Sn based anode alloys. *Int. J. Hydrogen Energy* **2017**, *42*, 11654−11661.
(29) Sun, Y.; Fu, C.; Ren, J.; Jiang, M.; Guo, M.; Cheng, R.; Zhang, J.; Sun, B. Highly Conductive and Reusable Electrolyte Based on Sodium Polyacrylate Composite for Flexible Al-Air Batteries. *J. Electrochem. Soc.* **2020**, *167*, 080502−080510.
(30) Ambat, R.; Davenport, A. J.; Scamans, G. M.; Afseth, A. Effect of iron-containing intermetallic particles on the corrosion behaviour of aluminium. *Corros. Sci.* **2006**, *48*, 3455−3471.
(31) Zhu, Y.; Sun, K.; Frankel, G. S. Intermetallic Phases in Aluminum Alloys and Their Roles in Localized Corrosion. *J. Electrochem. Soc.* **2018**, *165*, C807−C820.
(32) Qin, Y.-F.; Wang, S.-Q. Ab-Initio Study of the Role of Mg_2Si and Al_2CuMg Phases in Electrochemical Corrosion of Al Alloys. *J. Electrochem. Soc.* **2015**, *162*, C503−C508.
(33) Birbilis, N.; Buchheit, R. G. Electrochemical Characteristics of Intermetallic Phases in Aluminum Alloys. *J. Electrochem. Soc.* **2005**, *152*, B140.
(34) Curioni, M.; Scenini, F. The Mechanism of Hydrogen Evolution During Anodic Polarization of Aluminium. *Electrochim. Acta* **2015**, *180*, 712−721.
(35) Burstein, G. T.; Cinderey, R. J. Evolution of the corrosion potential of repassivating aluminium surfaces. *Corros. Sci.* **1992**, *33*, 475−492.
(36) Adhikari, S.; Hebert, K. R. Factors controlling the time evolution of the corrosion potential of aluminum in alkaline solutions. *Corros. Sci.* **2008**, *50*, 1414−1421.
(37) Park, I.-J.; Choi, S.-R.; Kim, J.-G. Aluminum anode for aluminum-air battery − Part II: Influence of In addition on the

https://dx.doi.org/10.1021/acssuschemeng.0c08415
ACS Sustainable Chem. Eng. 2021, 9, 2300−2308

electrochemical characteristics of Al-Zn alloy in alkaline solution. *J. Power Sources* **2017**, *357*, 47−55.
(38) Tang, Y.; Lu, L.; Roesky, H. W.; Wang, L.; Huang, B. The effect of zinc on the aluminum anode of the aluminum−air battery. *J. Power Sources* **2004**, *138*, 313−318.
(39) Ma, J.; Wen, J.; Gao, J.; Li, Q. Performance of Al−0.5 Mg−0.02 Ga−0.1 Sn−0.5 Mn as anode for Al−air battery in NaCl solutions. *J. Power Sources* **2014**, *253*, 419−423.
(40) Yin, X.; Yu, K.; Zhang, T.; Fang, H. J.; Dai, H.; Xiong, H. Q.; Dai, Y. L. Influence of Rolling Processing on Discharge Performance of Al-0.5Mg-0.1Sn-0.05Ga-0.05In Alloy as Anode for Al-air Battery. *Int. J. Electrochem. Soc.* **2017**, *12*, 4150−4163.
(41) Moghanni-Bavil-Olyaei, H.; Arjomandi, J.; Hosseini, M. Effects of gallium and lead on the electrochemical behavior of Al-Mg-Sn-Ga-Pb as anode of high rate discharge battery. *J. Alloys Compd.* **2017**, *695*, 2637−2644.
(42) Wang, D.; Zhang, D.; Lee, K.; Gao, L. Performance of AA5052 alloy anode in alkaline ethylene glycol electrolyte with dicarboxylic acids additives for aluminium-air batteries. *J. Power Sources* **2015**, *297*, 464−471.
(43) Wang, Q.; Miao, H.; Xue, Y.; Sun, S.; Li, S.; Liu, Z. Performances of an Al-0.15 Bi−0.15 Pb−0.035 Ga alloy as an anode for Al-air batteries in neutral and alkaline electrolytes. *RSC Adv.* **2017**, *7*, 25838−25847.

https://dx.doi.org/10.1021/acssuschemeng.0c08415
ACS Sustainable Chem. Eng. 2021, 9, 2300−2308